A Bidimensional Gay-Berne Calamitic Fluid: Structure and Phase Behavior in Bulk and Strongly Confined Systems

A. Calderón-Alcaraz[1], J. Munguía-Valadez[1], S. I. Hernández[2], A. Ramírez-Hernández[3], E. J. Sambriski[4] and J. A. Moreno-Razo[1]*

[1]Departamento de Física, Universidad Autónoma Metropolitana-Iztapalapa, Mexico City, Mexico, [2]Unidad Multidisciplinaria de Docencia e Investigación-Juriquilla, Facultad de Ciencias, Universidad Nacional Autónoma de México, Juriquilla, Querétaro, Mexico, [3]Department of Biomedical Engineering and Chemical Engineering, and Department of Physics and Astronomy, The University of Texas at San Antonio, San Antonio, TX, United States, [4]Department of Chemistry, Delaware Valley University, Doylestown, PA, United States

A bidimensional (2D) thermotropic liquid crystal (LC) is investigated with Molecular Dynamics (MD) simulations. The Gay-Berne mesogen with parameterization GB(3, 5, 2, 1) is used to model a calamitic system. Spatial orientation of the LC samples is probed with the nematic order parameter: a sharp isotropic-smectic (I-Sm) transition is observed at lower pressures. At higher pressures, the I-Sm transition involves an intermediate nematic phase. Topology of the orthobaric phase diagram for the 2D case differs from the 3D case in two important respects: 1) the nematic region appears at lower temperatures and slightly lower densities, and 2) the critical point occurs at lower temperature and slightly higher density. The 2D calamitic model is used to probe the structural behavior of LC samples under strong confinement when either planar or homeotropic anchoring prevails. Samples subjected to circular, square, and triangular boundaries are gradually cooled to study how orientational order emerges. Depending on anchoring mode and confining geometry, characteristic topological defects emerge. Textures in these systems are similar to those observed in experiments and simulations of lyotropic LCs.

Keywords: confinement, topological, disclination, transition, nematic, simulation

1 INTRODUCTION

Bulk materials exhibit properties imbued by their underlying chemical makeup: the packing of and interactions between atoms and/or molecules impart characteristic traits. On the other hand, *metamaterials* are synthetically produced and depend more on the relative positioning of building blocks within the structure. Such a trait allows metamaterials to achieve novel properties not exhibited by bulk materials (prominently of an electromagnetic and/or an optical nature). This has facilitated the expansion and miniaturization of existent technologies [1, 2].

Building blocks capable of molecular recognition are essential in the bottom-up production of metamaterials [3–7]. Specifically, complementary moieties can display the ability to "latch" in solution, onto a substrate, or in a combination of scenarios to produce desirable architectures. The threshold concentration of building blocks and formation steps are some issues to consider when optimizing their fabrication [8]. Structural properties in a metamaterial will remain stable provided the interaction strength between units withstands thermal fluctuations in the medium. Bottom-up approaches exploit this feature to circumvent the use of mechanical intervention. Production is

scaled by merely increasing the amounts of reactants and relying on system kinetics for product formation. Packing specificity can be modulated by carrying out the assembly under spatial confinement [9–15]. Many fabrication protocols have been optimized by mimicking the strategies latent in biomolecular systems [4, 16, 17].

The solvent is a key component in the production of metamaterials, which must effectively disperse building blocks and stabilize noncovalent interactions holding structures together. Self-assembly reliant on the chemical complementarity embedded in building blocks relegates the solvent to a passive role, serving in large measure as a dispersing agent. A paradigm shift is to screen solvents for an active role in the generation of metamaterials [18–22]. In this scenario, the solvent provides additional bottom-up control that extends the gamut of attainable targets [23–26].

The solvent "paradigm shift" is exemplified in the elastic forces mediated within a liquid crystal (LC) fluid. The intrinsic anisotropy of LCs facilitates spatially ordered mesophases. Solvent order at certain state points can be disturbed in the presence of colloidal inclusions, resulting in topological defects that exert static and dynamic control. Because of their ability to spatially "communicate," topological defects can couple (obeying topological charge rules) to yield specific colloidal arrangements, including dimers [27–38], wires (i.e., chains) [21, 28, 35, 39–44], and arrays [21, 31–34, 36–38, 43, 45, 46]. Solvents recruited as active agents contributing to the self-assembly of metamaterials enhance a variety of structural possibilities.

Much research has been devoted to three-dimensional (3D) self-assembly [25], though a two-dimensional (2D) variant continues to be of interest from an exploratory perspective [47–55] as well as in applied technologies [1, 56]. Optimal function is achieved *via* slab geometry in many devices, including optoelectronic/photonic materials [57–61], sensors [60, 62–68], display technologies [69–71], smart glass [72, 73], spatial light modulators [74–77], and tunable filters [78–81]. However, dimensionality plays an essential role in the type and extent of structural order that a condensed phase can maintain [52, 82–88]. When coupling the elastic forces of topological defects in LC media, colloidal ordering induced *via* a substrate can differ significantly from that observed *via* topological mediation in the bulk [21, 24, 25, 35, 36]. Slab assembly becomes relevant in 3D colloidal arrangements because it yields intermediates: metamaterials are finalized upon "stacking" slabs in layer-by-layer synthesis to achieve a target 3D structure [89–91].

In this work, we focus on two aspects of a thermotropic calamitic LC fluid relevant to colloidal self-assembly: 1) the changes in topology of the solvent phase diagram due to a reduction in dimensionality from 3D to 2D, and 2) the mesophase behavior of the solvent under strong confinement in slab geometry. The Gay-Berne (GB) model [92] is used here because it captures salient mesogenic features and has a relatively low computational overhead. Prior work with the GB mesogen has focused on different mesophases in bulk 3D systems [93–98]. Additionally, surface-induced ordering (i.e., anchoring) *via* boundary walls has been studied in thin films [99], droplets
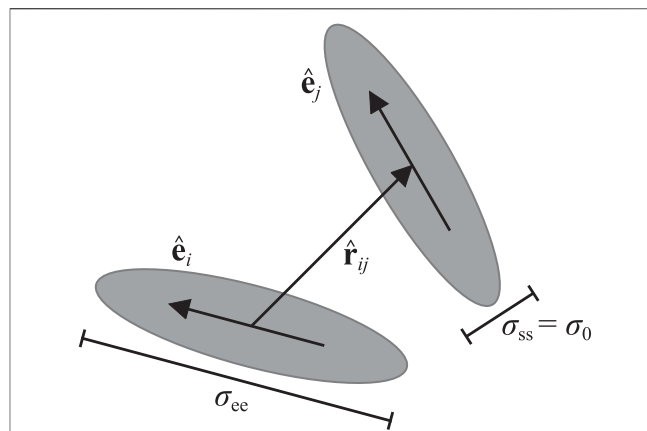

FIGURE 1 | Schematic defining the degrees of freedom and parameters associated with the GB (3, 5, 2, 1) mesogens. Molecular axes are defined by unit vectors $\hat{\mathbf{e}}_i$ and $\hat{\mathbf{e}}_j$. The center-to-center unit vector $\hat{\mathbf{r}}_{ij}$ tempers the interaction potential relative to mesogen-mesogen orientation, affecting both length [**Eq. 2**] and energy [**Eq. 5**] scales. The interaction potential is scaled by a model length σ_0 defined with respect to the side-side length σ_{ss}. The end-end length σ_{ee} is used to define the molecular aspect ratio; for the parameterization used in this work, $\sigma_{ee}/\sigma_{ss} = 3$.
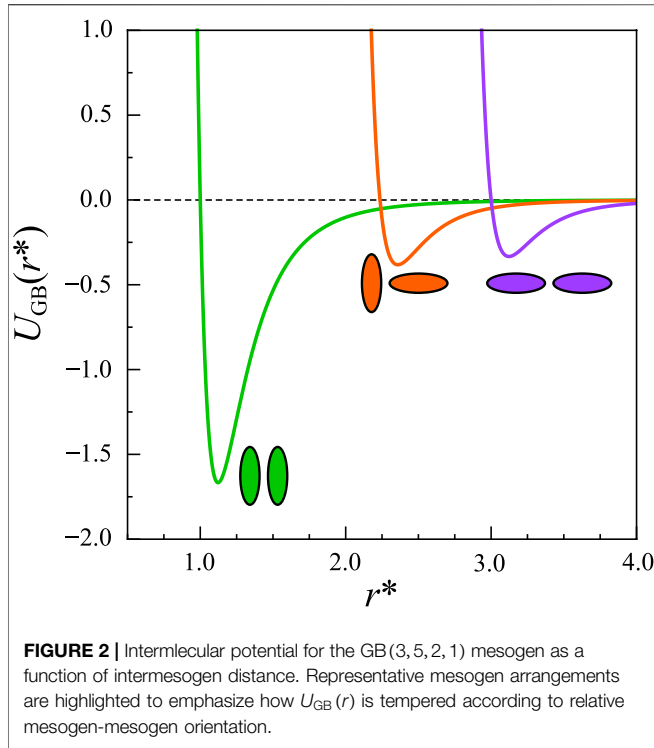
[100], and toroidal cavities [101]. Several GB parameterizations have reproduced nematic and smectic phases [102–104]. More recently, a discotic parameterization has been used to explore nematic and columnar phases [105–109], providing insight on structural and dynamic measurements at the molecular level [110–112]. The recognition of specific design principles has stimulated the attainment of novel targets [27].

Despite serving as a point of reference for 3D phenomena, the phase behavior of a strictly 2D thermotropic GB LC system has been limited [113, 114]. On the experimental front, optical microscopy commonly provides information on quasi-2D samples, and in most cases, data merely reflect 2D projections of an underlying 3D system [56, 115]. Renewed interest in the organization of rigid biopolymers as effective 2D systems (in bulk and under confinement) has led to new and interesting textures observed under strong confinement [116–122]. Simple simulation models reproduced the phenomenology observed in 2D [123–126]. Because those efforts focused on lyotropic liquid crystals, we extend the field by considering a thermotropic fluid. Specifically, we explore how shape of the confining area and type of anchoring induced by boundary walls affect mesophase behavior.

2 MODEL AND METHODS

The GB model is a generalization of the Lennard-Jones potential defining the interaction between anisotropic molecules. Each molecule i is represented as an ellipsoid having a center-of-mass position $\mathbf{r}_i$ and a unit vector $\hat{\mathbf{e}}_i$ along the principal (major) axis denoting its orientation (**Figure 1**).

The intermolecular interaction between the ith and jth mesogens is written as

FIGURE 2 | Intermlecular potential for the GB$(3, 5, 2, 1)$ mesogen as a function of intermesogen distance. Representative mesogen arrangements are highlighted to emphasize how $U_{GB}(r)$ is tempered according to relative mesogen-mesogen orientation.

$$U_{GB}(\mathbf{r}_{ij}, \widehat{\mathbf{e}}_i, \widehat{\mathbf{e}}_j) = 4\,\varepsilon(\widehat{\mathbf{r}}_{ij}, \widehat{\mathbf{e}}_i, \widehat{\mathbf{e}}_j) \left[\Xi_{ij}^{-12} - \Xi_{ij}^{-6} \right], \tag{1}$$

where $\mathbf{r}_{ij} = \mathbf{r}_i - \mathbf{r}_j$ and the scaled distance is given by

$$\Xi_{ij} = \frac{1}{\sigma_0} \left[\mathbf{r}_{ij} - \sigma(\widehat{\mathbf{r}}_{ij}, \widehat{\mathbf{e}}_i, \widehat{\mathbf{e}}_j) + \sigma_0 \right], \tag{2}$$

where σ_0 the width of the mesogen (i.e., the minor axis) and $\mathbf{r}_{ij} = |\mathbf{r}_{ij}|$ is the magnitude of the intermolecular (center-to-center) separation vector. The relative orientation of mesogens within the medium must be taken into account to regulate the strength of the intermesogen interaction. This requires a fully specified function of a general variable ω,

$$\Gamma(\omega) = 1 - \omega \left[\frac{c_i^2 + c_j^2 - 2\,\omega\,c_i\,c_j\,c_{ij}}{1 - \omega^2\,c_{ij}^2} \right], \tag{3}$$

where $c_i = \widehat{\mathbf{e}}_i \cdot \widehat{\mathbf{r}}_{ij}$, $c_j = \widehat{\mathbf{e}}_j \cdot \widehat{\mathbf{r}}_{ij}$, $c_{ij} = \widehat{\mathbf{e}}_i \cdot \widehat{\mathbf{e}}_j$, and $\widehat{\mathbf{r}}_{ij} = \mathbf{r}_{ij}/|\mathbf{r}_{ij}|$ is the unit (center-to-center) separation vector. The orientation-dependent length scale (range) parameter $\sigma(\widehat{\mathbf{r}}_{ij}, \widehat{\mathbf{e}}_i, \widehat{\mathbf{e}}_j)$ is computed as

$$\sigma(\widehat{\mathbf{r}}_{ij}, \widehat{\mathbf{e}}_i, \widehat{\mathbf{e}}_j) = \sigma_0 \left[\Gamma(\chi) \right]^{-1/2} \tag{4}$$

Here, $\chi = (\kappa^2 - 1)/(\kappa^2 + 1)$, where $\kappa = \sigma_{ee}/\sigma_0 = \sigma_{ee}/\sigma_{ss}$ is the length-to-width (aspect) ratio of the mesogen (**Figure 1**). The strength anisotropy function $\varepsilon(\widehat{\mathbf{r}}_{ij}, \widehat{\mathbf{e}}_i, \widehat{\mathbf{e}}_j)$ is defined by the product

$$\varepsilon(\widehat{\mathbf{r}}_{ij}, \widehat{\mathbf{e}}_i, \widehat{\mathbf{e}}_j) = \varepsilon_0 \left[\varepsilon_1(\widehat{\mathbf{e}}_i, \widehat{\mathbf{e}}_j) \right]^{\nu} \left[\varepsilon_2(\widehat{\mathbf{r}}_{ij}, \widehat{\mathbf{e}}_i, \widehat{\mathbf{e}}_j) \right]^{\mu}, \tag{5}$$

where the exponents ν and μ are adjustable parameters. The energy anisotropy functions are defined as

$$\varepsilon_1(\widehat{\mathbf{e}}_i, \widehat{\mathbf{e}}_j) = \left[1 - \chi^2(\widehat{\mathbf{e}}_i \cdot \widehat{\mathbf{e}}_j)^2 \right]^{-1/2} \tag{6}$$

and

$$\varepsilon_2(\widehat{\mathbf{r}}_{ij}, \widehat{\mathbf{e}}_i, \widehat{\mathbf{e}}_j) = \Gamma(\chi'). \tag{7}$$

The parameter χ' depends on the ratio of the potential well depths corresponding to side-side (ss) and end-end (ee) configurations, $\kappa' = \varepsilon_{ss}/\varepsilon_{ee}$. More specifically, $\chi' = [(\kappa')^{1/\mu} - 1]/[(\kappa')^{1/\mu} + 1]$.

The GB model uses four parameters conventionally represented as $GB(\kappa, \kappa', \mu, \nu)$. Previous work has shown that specific parameter sets reproduce thermodynamic and structural properties of experimental systems [105, 107, 127]. A complete phase diagram of the 3D GB model is available for $GB(3, 5, 2, 1)$ [104, 128–132], which corresponds to a calamitic mesogen. Moreover, this parameterization has been used to investigate intermolecular interactions in nematic samples [133–135]. Simulations have been previously reported for GB discotic mesogens focused on tracing changes in phase behavior under confinement [99, 130, 136–140] and in droplets [141]. The reader interested in additional parameterizations is referred to previous work [127, 129, 135, 142–146].

The $GB(3, 5, 2, 1)$ parameterization is used in this work to elucidate the role that dimensionality plays on mesophase behavior. Shown in **Figure 2** are representative interaction energy curves as a function of intermesogen distance for different relative orientations. For the $GB(3, 5, 2, 1)$ mesogen, the side-side arrangement is preferred over other configurations, a feature that promotes the nematic phase at reasonably accessible temperatures. The $GB(3, 5, 2, 1)$ parameterization was chosen because it has been extensively used as a model for prolate LCs, such as the alkylbiphenyl mesogen family.

Confined systems were modeled with walls constructed from an array of spherical (i.e., circular in 2D) particles. The mesogen-wall interaction is obtained by taking the limit of **Eqs. 1** and **2** when one of the interacting mesogens becomes a sphere (i.e., a wall particle) [147–149]. In that limit, the range parameter and strength anisotropy functions are given by

$$\sigma_w(\widehat{\mathbf{r}}_{ij}, \widehat{\mathbf{e}}_j) = \sigma_0 \left[1 - \chi(\widehat{\mathbf{r}}_{ij} \cdot \widehat{\mathbf{e}}_j)^2 \right]^{-1/2} \tag{8}$$
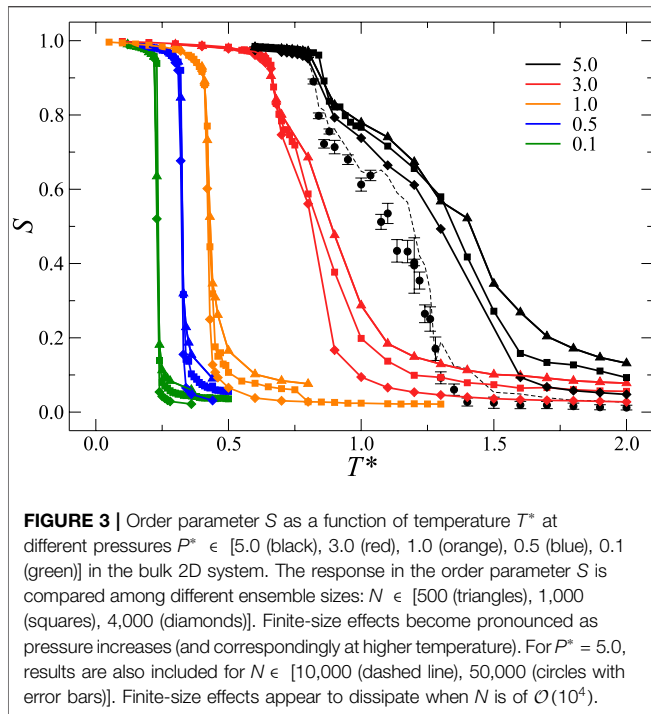
and

$$\varepsilon_w(\widehat{\mathbf{r}}_{ij}, \widehat{\mathbf{e}}_j) = \varepsilon_0 \left[1 - \chi'_w(\widehat{\mathbf{r}}_{ij} \cdot \widehat{\mathbf{e}}_j)^2 \right] \tag{9}$$

where

$$\chi'_w = 1 - (\varepsilon_h/\varepsilon_p)^{1/\mu}. \tag{10}$$

For **Eqs. 8–10**, the ith molecule denotes a wall-type particle, the jth molecule refers to a mesogen, ε_h corresponds to the energy scale for *homeotropic* anchoring (when $\widehat{\mathbf{e}}_j$ is locally perpendicular to the confining wall), and ε_p represents the energy scale for

FIGURE 3 | Order parameter S as a function of temperature T^* at different pressures $P^* \in$ [5.0 (black), 3.0 (red), 1.0 (orange), 0.5 (blue), 0.1 (green)] in the bulk 2D system. The response in the order parameter S is compared among different ensemble sizes: $N \in$ [500 (triangles), 1,000 (squares), 4,000 (diamonds)]. Finite-size effects become pronounced as pressure increases (and correspondingly at higher temperature). For $P^* = 5.0$, results are also included for $N \in$ [10,000 (dashed line), 50,000 (circles with error bars)]. Finite-size effects appear to dissipate when N is of $\mathcal{O}(10^4)$.

planar anchoring (when $\hat{\mathbf{e}}_j$ is locally parallel to the confining wall). Anchoring conditions can thus be controlled by adjusting these two parameters.

We focus on a strictly 2D thermotropic liquid crystal in this work: "flat" ellipsoidal mesogens evolve in a plane. All results reported herein were generated by performing MD simulations in the canonical (*NAT*, where A is constant area for 2D, analogous to *NVT* where V is constant volume in 3D) and isothermal-isobaric (*NPT*) ensembles. Translational and rotational equations of motion were integrated using the velocity-Verlet algorithm [150]. For bulk samples, in either the *NAT* or *NPT* ensembles, the time step used was $\delta t = 0.001$. For systems in confined regions, the time step used was $\delta t = 0.002$. The coupling parameters for simulations were as follows: $Q_{\text{thermostat}} = 10$, $Q_{\text{barostat}} = 1,000$. In the case of bulk samples, the simulation cell was defined with lateral dimensions L_x and L_y: periodic boundary conditions were applied in all directions. All simulations were initialized at relatively high temperature (i.e., $T^* = k_B T/\varepsilon_0 = 1.0$). Low-temperature states ($T^* = k_B T/\varepsilon_0 = 0.1$) were attained by cooling the system gradually. Velocities were assigned from a Maxwell-Boltzmann distribution and the moments of inertia were set to $I = (\sigma_0^2/20)(\kappa^2 + 1)$ [151]. All particles were set to unit mass ($m = 1$) and intermolecular potentials were truncated at a cutoff length scale $r_c = (\kappa + 1)\sigma_0$ for expediency. Interparticle potentials were shifted to enforce a smoothly vanishing force at r_c. Simulations were run for at least 5×10^6 time steps for equilibration and another 5×10^6 time steps for production.

Global orientational order is characterized by the orientational traceless tensor $\mathbf{Q}$ [152], specialized for the 2D case [153] as

$$\mathbf{Q} = \frac{1}{N} \sum_{i=1}^{N} (2\hat{\mathbf{e}}_i \otimes \hat{\mathbf{e}}_i - \mathbf{I}), \tag{11}$$

where $\otimes$ denotes the tensor product and $\mathbf{I}$ is the identity matrix. Diagonalization of $\mathbf{Q}$ leads to two eigenvalues (λ_+ and λ_-). The nematic (Maier-Saupe) order parameter S is defined in terms of the highest eigenvalue λ_+, so that $S = \lambda_+$. The parameter S is equal to zero for isotropic configurations and increases as orientational order increases.

3 RESULTS AND DISCUSSION

3.1 Orientational Order and Liquid Structure

In this section, we present data for a series of samples of increasing size (mesogen number) to elucidate the orientational order of the LC liquid as a function of temperature. We focus here on characterizing differences due specifically to sample size, considering $N \in \{500, 1000, 4000\}$. Profiles for the Maier-Saupe order parameter are presented in **Figure 3**.

The nematic order parameter S displays a state with low orientational order ($S \approx 0$) when the temperature exceeds a threshold depending on the pressure P^* of the system. The onset of orientational order shows a jump in S, such that $S \approx 1$ when the temperature is sufficiently low: this high value of S indicates the formation of the smectic phase. An isotropic-smectic transition (I-Sm) takes place without an intermediate nematic state when the pressure is sufficiently low (i.e., for $P^* < 2$). As the pressure increases, the I-Sm transition occurs by passing through a range of nematic state points, corresponding approximately to $0.25 < S < 0.75$. A finite-size effect in S becomes pronounced at higher pressure (i.e., $P^* \gtrsim 2$): the transition appears less sharp as the ensemble size N decreases.

To investigate how finite-size effects are pronounced at higher pressures, simulations were performed for $P^* = 5.0$. At this pressure, finite-size effects are accentuated. We performed simulations for $N \in \{10000, 50000\}$. As can be gleaned from **Figure 3**, results for the larger two systems are close to one another. Hence, finite-size effects seemingly dissipate when the ensemble size is at least of $\mathcal{O}(10^4)$.

To gain insight into the local structure, we analyzed MD snapshots for $N = 50,000$ when $P^* = 5.0$ *via* a temperature sweep shown in **Figure 4**. An eightfold magnification of a portion of the ensemble is shown to aid discerning local mesophase order: the entire ensemble for each temperature is provided in the **Supplementary Material**. At high temperatures, translational entropy overwhelms the cohesive energy of the LC medium and a disordered phase is the most stable state accessible to the system. At intermediate temperatures, the ensemble displays small clusters of mesogens with correlated orientation. Clustering grows in spatial extent with decreasing temperature. At even lower temperatures, the cohesive energy overtakes the decreasing translational entropy: a liquid phase with smectic order ensues at these temperatures. The smectic mesophase is stabilized
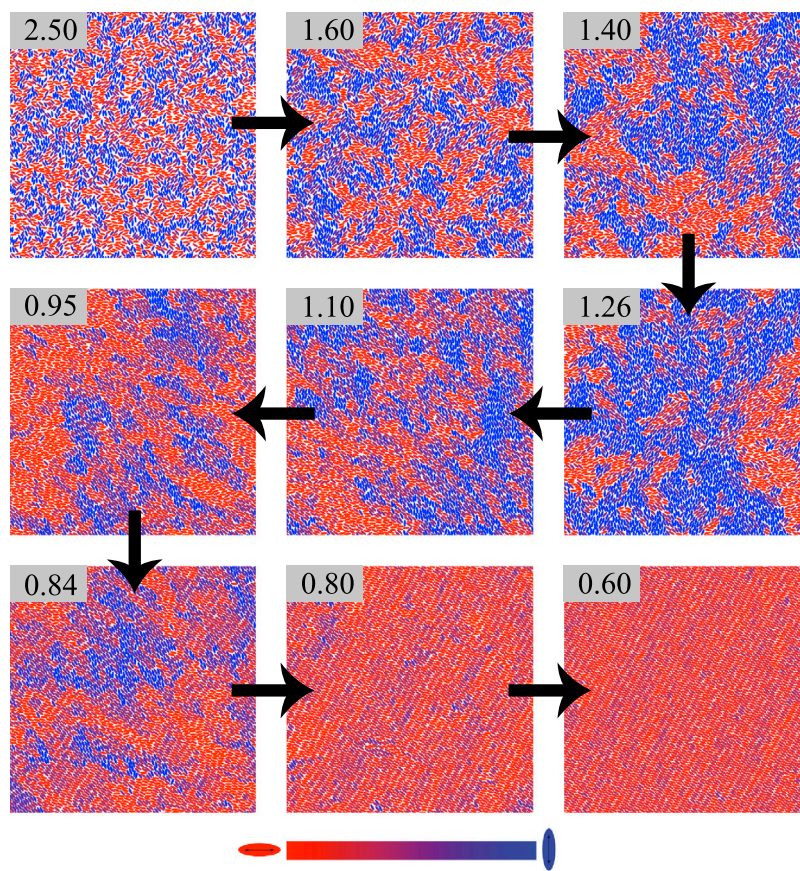
FIGURE 4 | Snapshots of the bulk 2D system when $P^* = 5.0$ and $N = 50,000$. Shown is an eightfold-magnified region of the ensemble to discern the local order of mesogens. Configurations are arranged as a temperature sweep (arrows) with each configuration showing its temperature T^*. Mesogens are colored according to orientation, as indicated by the color bar (bottom).

(i.e., structural order increases in spatial extent) upon further cooling.

3.2 Phase Diagram Topology and Mesophases

A major contribution in this study is the orthobaric [i.e., (ρ^*, T^*)] phase diagram for the 2D system shown in **Figure 5**. The 3D case for the same GB mesogen is overlaid with gray and red shadows: such a comparison enables us to appreciate how dimensionality affects topology. The phase diagram for the 3D case was previously reported [128, 129]. The 2D phase diagram reported here was obtained from MD simulations performed in the isothermal-isobaric (*NPT*) ensemble. The pressure P^* was controlled with a Nosé-Hoover barostat; samples consisted of $N = 1,000$ mesogens. Phase regions were outlined by acquiring data for $P^* \in \{0.1, 0.5, 1.0, 2.0, 3.0, 5.0\}$. For each pressure, the system was initialized at a high temperature and gradually cooled in steps of $\Delta T^* = 0.02$ for at least 5×10^6 time steps.

When compared to the 3D case, the 2D system displays an evident shift in its phase boundaries. This behavior is justified by

the fact that thermal fluctuations are stronger when the dimensionality of the system is reduced [154–156]. The 2D system shows that the nematic phase emerges over a wider (nearly double) range in temperature at slightly lower densities. Additionally, the isotropic phase occupies a larger area of stability in the (ρ^*, T^*)-plane, extending to lower temperatures and higher densities in 2D. The critical point appears at a lower temperature ($T_c^* = 0.202 \pm 0.007$) and slightly higher density ($\rho_c^* = 0.159 \pm 0.002$) when compared to the 3D system. Our result for the 2D critical point compares very well with previous work [157, 158].

It is instructional to consider how finite-size effects influence the topology of the phase diagram. For this purpose, three isobars are included: $P^* \in \{0.1, 3.0, 5.0\}$. For the (ρ^*, T^*) region shown, only slight deviations from the boundaries in the top-right corner would be expected. Boundaries shown on the phase diagram serve as a guide to the eye based on the available data extracted from the isothermal-isobaric simulations. The slim regions conveyed by solid lines are best estimates that outline the limits of phase stability and do not represent true coexistence lines.

We note that isothermal-isobaric simulations can probe metastable regions that elude canonical simulations without
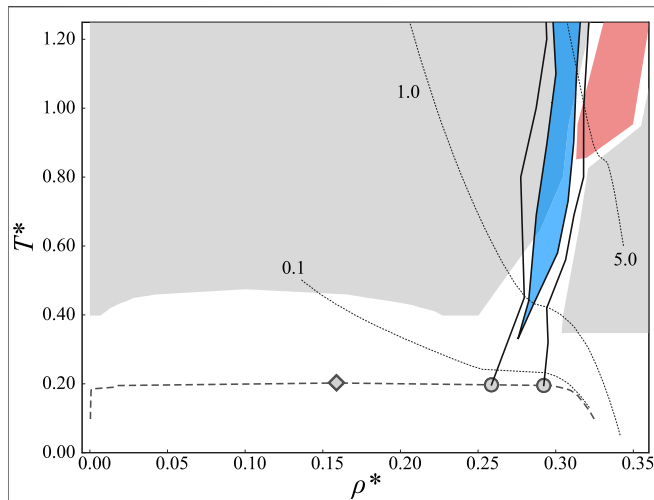
FIGURE 5 | The orthobaric phase diagram for the GB $(3, 5, 2, 1)$ mesogen in 2D (lines) and 3D (gray shadow). The 2D critical point (diamond) appears when $\rho_c^* = 0.159 \pm 0.002$ and $T_c^* = 0.202 \pm 0.007$. The nematic phase region is highlighted in both cases: 2D (blue shadow) and 3D (red shadow). For 2D, the nematic region is stable over a wider T^*-range for a slightly narrower ρ^*-range. Three specific isobars (dotted lines, labeled with P^*) are shown for comparison. Only the top-right region of the phase diagram is most sensitive to finite-size effects as shown in the response of the order parameter S in **Figure 3**.

yielding coexistence (i.e., phase separation). The complete mapping of such phase boundaries would require free energy calculations, such as Gibbs ensembles [159–161], Gibbs-Duhem integration [162], histogram reweighting [163], or the Frenkel-Ladd method [164], among others. The coexistence of mesophases, however, was verified by independent canonical simulations. A sample cooling routine highlighting the coexistence of different mesophases is shown in **Figure 6**. The snapshots trim out sparsely populated regions of the full simulation cell observed at lower temperatures.

3.3 Confinement: Point Defects and Domain Walls

The extent to which mesophase structure is affected by strong confinement was also explored in this study. Inspiration for this lies in the rich structures and topological defects observed in lyotropic systems: the similarity in the textures observed in our thermotropic system highlights certain universal traits of topological defects. From an applications standpoint, this is of interest because topological defects can be recruited for the self-ordering of colloidal particles. In the case of a 2D system, this arrangement has the potential to yield monolayers of colloidal particles with specific positional constraints.

The 2D LC samples were confined within walls consisting of an array of fixed Lennard-Jones particles. Three different confinement scenarios were considered in this study: circular, square, and triangular. The mesogen packing fraction was kept approximately at $\eta = 0.75$ in all cases to ensure a nematic state point consistent with the bulk 2D phase diagram. As a point of
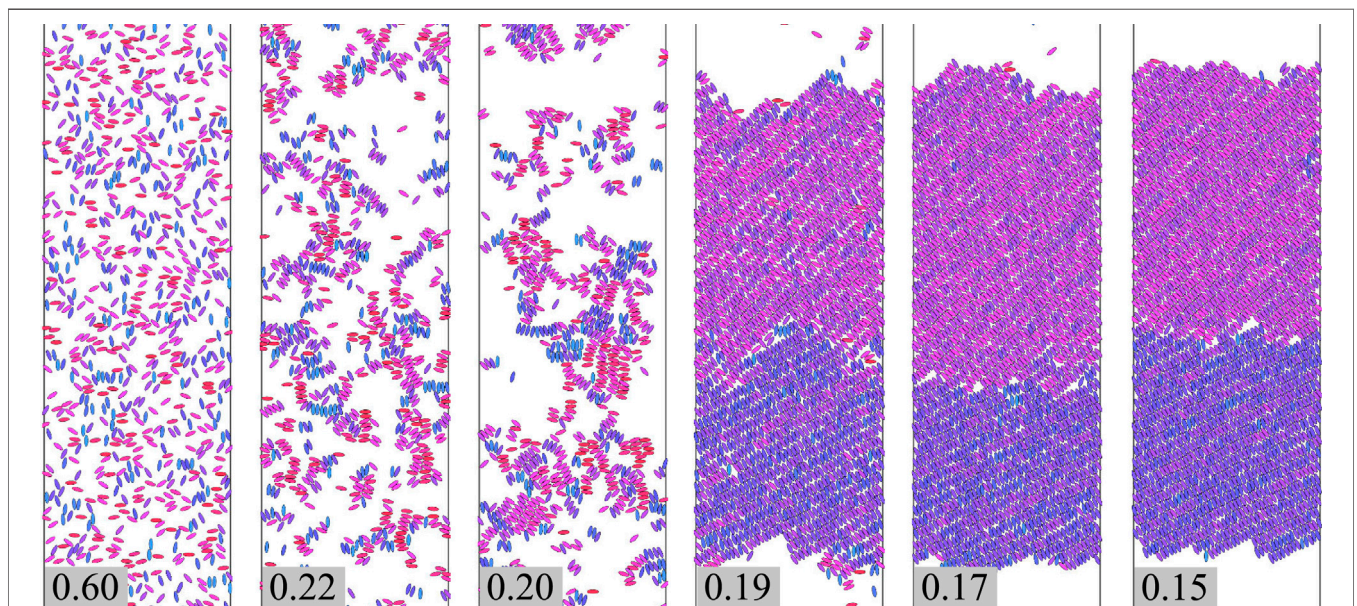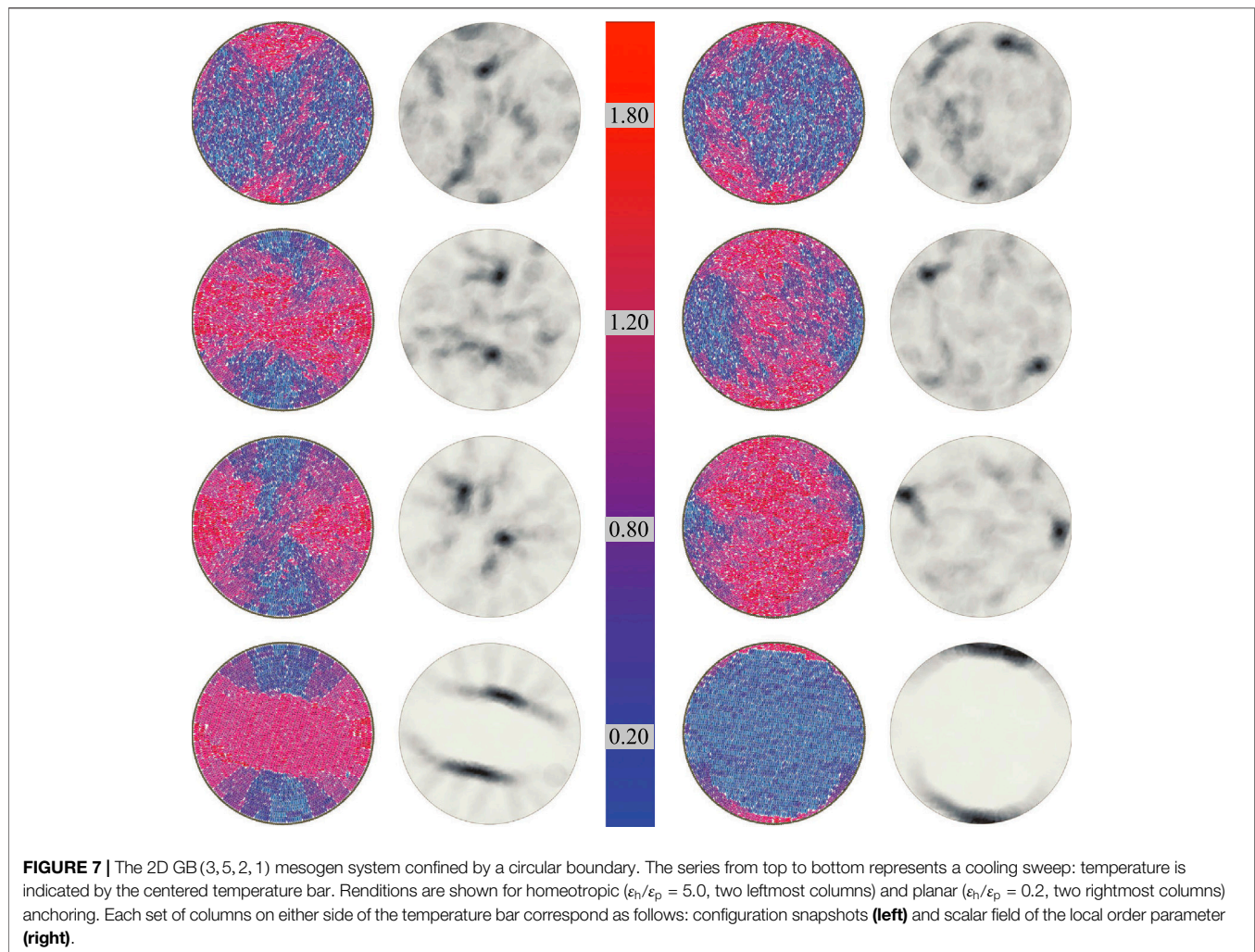

FIGURE 6 | A representative cooling sweep in the *NAT* ensemble. Configurations are shown for an ensemble with $N = 2,000$ and $\rho^* = 0.10$. The temperature T^* decreases going from left to right over a narrow temperature window as shown. Snapshots of the simulation box have been trimmed to improve the visual clarity of the more densely populated regions observed at lower temperature.

FIGURE 7 | The 2D GB(3, 5, 2, 1) mesogen system confined by a circular boundary. The series from top to bottom represents a cooling sweep: temperature is indicated by the centered temperature bar. Renditions are shown for homeotropic ($\varepsilon_h/\varepsilon_p = 5.0$, two leftmost columns) and planar ($\varepsilon_h/\varepsilon_p = 0.2$, two rightmost columns) anchoring. Each set of columns on either side of the temperature bar correspond as follows: configuration snapshots **(left)** and scalar field of the local order parameter **(right)**.
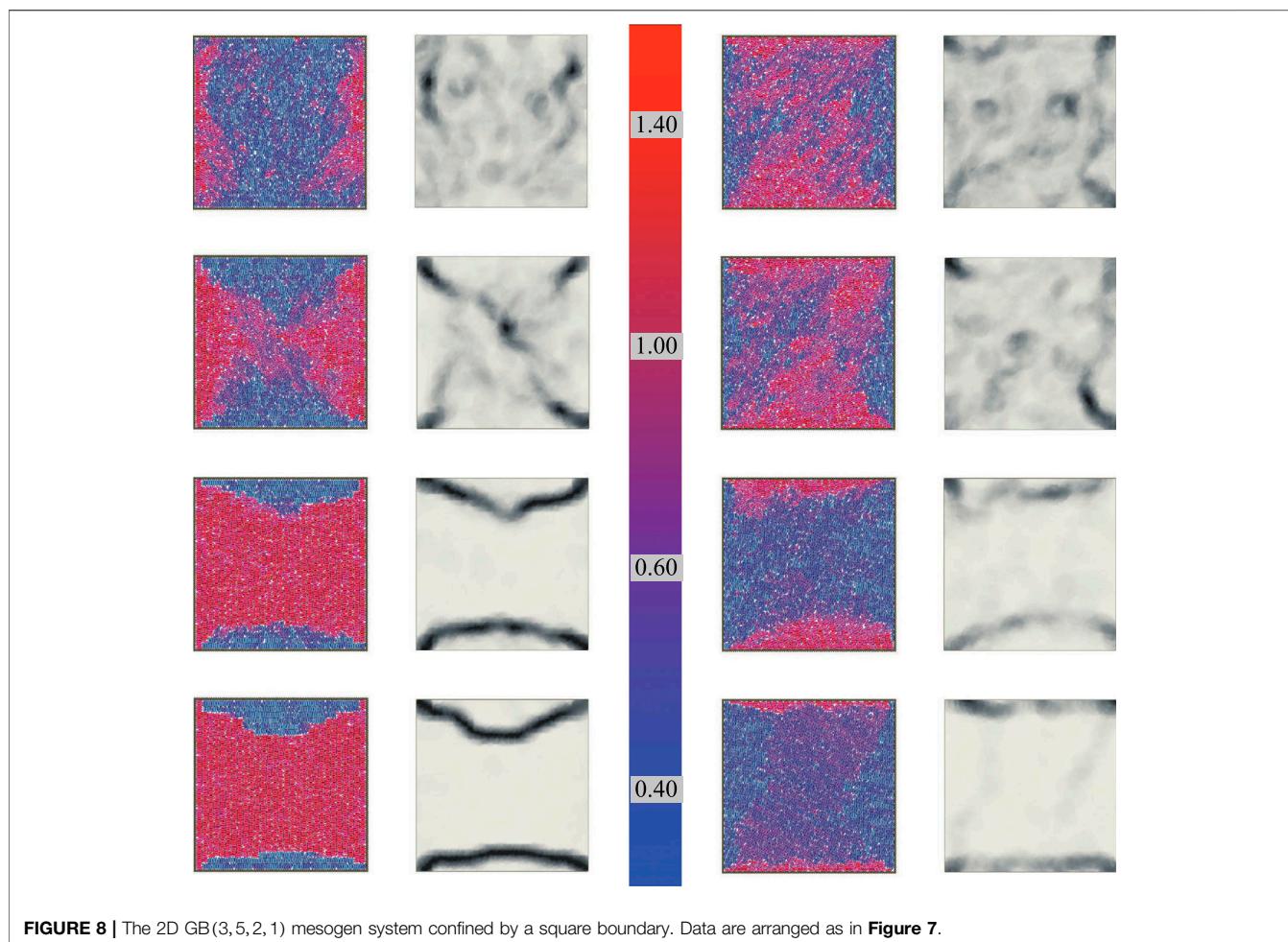
reference, the packing fraction for a 2D hexagonal lattice composed of circular units is $\eta \approx 0.907$ [165].

To characterize the way the confining walls exert a structuring effect on the mesogenic liquid, two anchoring conditions were considered: *homeotropic* ($\varepsilon_h/\varepsilon_p = 5.0$) and *planar* ($\varepsilon_h/\varepsilon_p = 0.2$) cases (**Eq. 10**). The nematic field emerging from the sample in the bulk region displays a dominant direction. However, the boundaries defining the confined area disrupt any such dominant alignment. The resulting director field persists in response to a delicate balance between anchoring conditions imposed by the confining walls and the strong tendency of neighboring mesogens to mutually align. As a result, this synergy has the effect of stabilizing topological defects within the confined region.

Data for circular confinement are shown in **Figure 7**. Topological defects are sharply sensitive to the type of anchoring. For homeotropic anchoring, the confinement radius in this work affords a low-temperature director field giving rise to two defects (with topological charge +1/2), localized away from the wall but separated in relation to one another. This behavior is consistent with density functional

theory predictions [119]. As temperature increases, the defects move away from one another until they approach the wall: at sufficiently high temperature ($T^* \sim 1.80$), the defects dissipate to yield a single, isotropic configuration. Such an outcome is possible because the anchoring energies at the confining surfaces are of finite strength. As can be seen in the configuration snapshots, thermal fluctuations are sufficiently strong to overcome the orientation induced by anchoring.

The situation changes for planar anchoring: at low temperature, two defects are present, but they are located at opposite poles of the confining circle. As a result, the so-called polar nematic configuration is observed. This state is distinguished by a layered mesophase similar to the smectic-like state that dominates all but two thin surface shells on opposite ends ($T^* \sim 0.20$). Another configuration also observed at the lowest temperature possesses boundary disclinations, but the main topological defect consists of point defects appearing on opposite poles of the circular boundary (refer to the discussion on circular boundary confinement in **Section 3.4**). Radially oriented domains, like those observed in the case of homeotropic anchoring, are absent in planar

FIGURE 8 | The 2D GB $(3, 5, 2, 1)$ mesogen system confined by a square boundary. Data are arranged as in **Figure 7**.
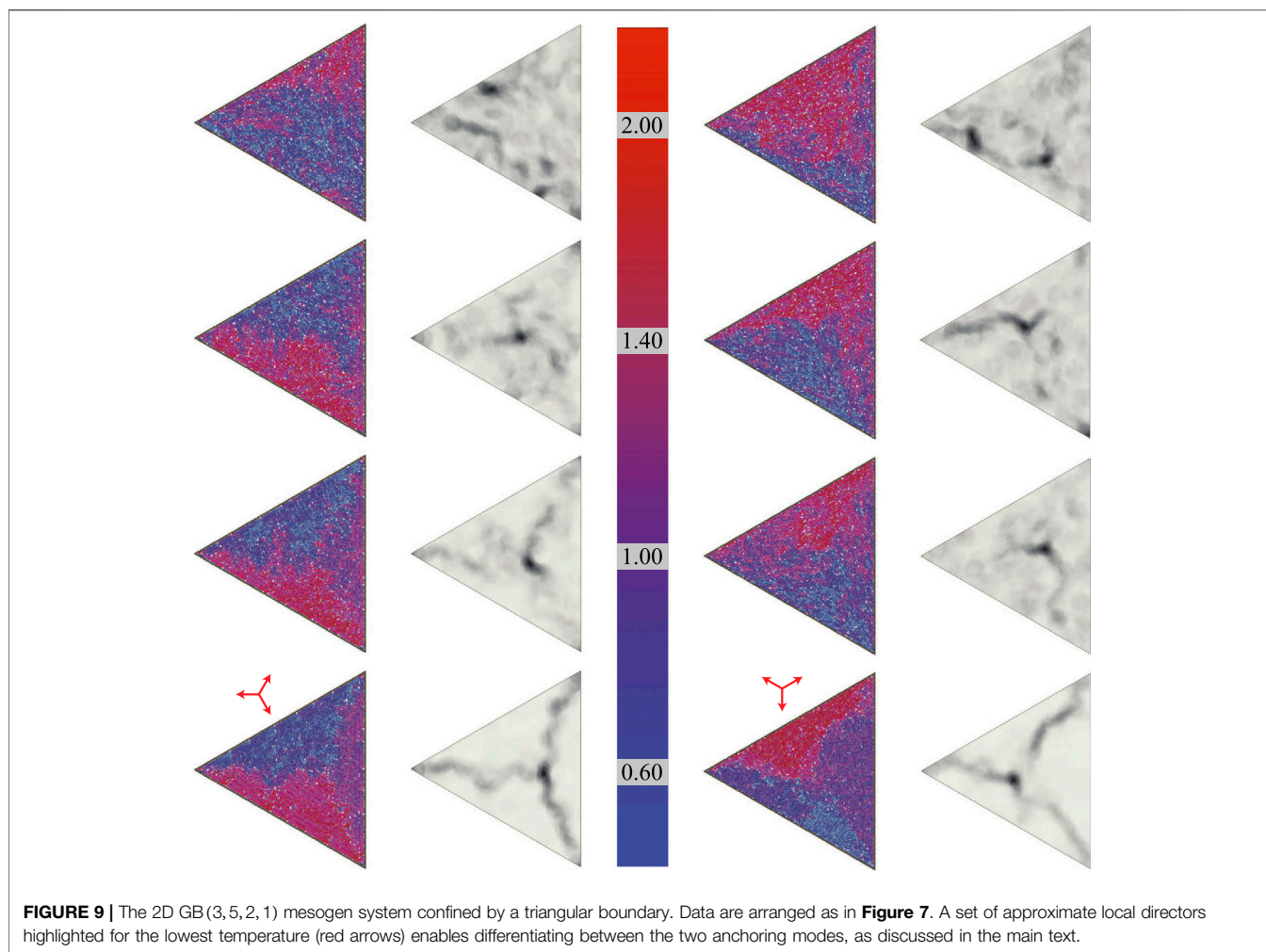
anchoring. Nematic-like order emerges as temperature increases for both anchoring modes under circular confinement. Although two polar defects persist at high temperature in the two systems ($T^* \sim 1.20$), the type of anchoring can be distinguished by probing the relative distance between defects: the separation between the two defects is always larger (nearing the boundary wall) for planar anchoring. As expected, internal order is mostly lost in both types of anchoring at sufficiently high temperatures. Our observations are consistent with those documented for a 2D fluid of hard rods in the high-density regime, with a sufficiently small aspect ratio [124].

Square confinement leads to more interesting textures as shown in **Figure 8**. The reduced symmetry of the boundary frustrates global mesophase order. For both anchoring conditions, domain walls (i.e., boundaries between different orientationally ordered domains) appear at sufficiently low temperature ($T^* \sim 0.60$). For homeotropic anchoring, domain walls define three regions: a large region with a local director rotated $\pi/2$ radians in relation to the local directors characterizing two small regions oriented in the same direction. Mesogens in the large region are highly oriented and form smectic-like layers. These domain walls signal domains possessing different orientations: the free energy is minimized in the system when

curved interfaces develop. Moreover, two equivalent states are possible by symmetry: one shown in the snapshots and another obtained by rotating the snapshot $\pi/2$ radians. In this way, the system displays two-fold degeneracy. This effect was previously observed using a density-functional approach [166]. An external field can lead to an interchange between the two states dynamically, as previously reported [167].

When planar anchoring is operative under square confinement, four domain walls (i.e., five regions) appear. Four small regions display an orientation aligned with the confining walls and one interior region with a local director tilted slightly in relation to adjacent lateral domains. This arrangement is strikingly similar to the $W \sim 40L$ system studied by Cortes et al. [117]. It is plausible for the interior region to eventually reorient to create a single region where the local director matches that of two adjacent lateral domains. As temperature increases, those domain walls disappear and two point defects arise close to the corners of the square. The structural behavior of the LC sample under square confinement agrees with previous theoretical models [121].

The most severe confining geometry in this study is the triangular boundary, the results of which are shown in **Figure 9**. For either type of anchoring, three orientationally

FIGURE 9 | The 2D GB $(3, 5, 2, 1)$ mesogen system confined by a triangular boundary. Data are arranged as in **Figure 7**. A set of approximate local directors highlighted for the lowest temperature (red arrows) enables differentiating between the two anchoring modes, as discussed in the main text.

ordered regions are discernible at low temperature: the resulting topological defects are driven by an order that permeates from the boundary wall toward the center of the confining region. This effect promotes the formation of a near-centered defect in either anchoring case at fairly high temperature ($T^* \sim 2.00$). Streak disclinations radiate from the point defect, signaling the partition between distinctly oriented regions giving rise to three domain walls only when the temperature is sufficiently low ($T^* \sim 0.60$).

Although the scalar fields of the order parameter under triangular confinement for both anchoring cases are similar, the two samples can still be differentiated when accounting for local order. The approximate local directors corresponding to the three oriented domains highlighted in **Figure 9** are rotated $\pi/6$ radians with respect to one another. This difference arises from the coupling of the anisotropic shape of the calamitic mesogen and the underlying confining geometry. When placed at the center of the triangular region, the set of directors for the homeotropic sample point at the corners of the triangular boundary; the analogous set for planar anchoring results in the bisection of all sides of the triangular region. As expected, the orientationally ordered regions and the streak

disclinations dissipate with increasing temperature, though the point defect persists even at high temperature ($T^* \sim 1.40$).

3.4 Dynamics of Confined Samples

Ancillary data from this work are ensemble trajectories given that systems were evolved with MD simulations. Although static information obtained from simulation snapshots is useful in characterizing orientational order and topological defects, it is equally important to probe the temporal behavior of mesophases. To this end, trajectories were leveraged to probe dynamical fluctuations in the fluid structure and the scalar field of the order parameter. The **Supplementary Material** includes trajectory visualizations for the systems in **Figures 7–9**. Each visualization is labeled by temperature and anchoring mode. The timescale in each case corresponds to approximately 3% of an entire simulation run.

The system under circular confinement with planar anchoring at reasonably high temperatures already exhibits features reminiscent of the polar defects stabilized at low temperatures. However, such defects are accompanied by strong fluctuations in intensity and positional alignment. As one point defect vanishes another emerges in the same pole. For homeotropic anchoring, point defects fluctuate in number, intensity, and position at high

temperatures. Upon further cooling, the homeotropic sample displays two point defects with minimal fluctuations in position and intensity, immediately after two radially oriented domains form. Before the central smectic-like region sets in, the separation between the two point defects reaches a minimum. Fluctuations in intensity are minimal at the lowest temperature studied: the separation between point defects stabilizes at a slightly larger distance ($T^* \sim 0.20$) than before ($T^* \sim 0.80$). In the case of planar anchoring, point defects appear on opposite poles of the circular boundary. Unlike the low-temperature configuration in **Figure 7**, textures in the bulk region of the confined area become richer when the smectic phase sets in: boundary defects of fleeting intensity appear upon further cooling for planar anchoring. However, polar defects persist prominently.

The behavior of topological defects upon sample cooling is similar for both anchoring modes under square confinement. In both cases, a highly fluctuating cross pattern with approximately two point-like defects on opposite corners of the square is observed. As soon as the sample reaches a temperature where the smectic mesophase becomes favorable, the fleeting point-like defects vanish: each anchoring case becomes distinguishable at this point ($T^* \sim 0.60$). For homeotropic anchoring, two prominent domain walls persist, giving rise to three distinct regions. For planar anchoring, four domain walls become stable, demarcating five distinct regions. The domain walls, although subdued when compared to the homeotropic case, yield a rhomboidal pattern.

When comparing the two anchoring modes for triangular confinement, the cooling history is very similar in both cases. A point defect is characteristic of either case upon the slightest hint of ordering. Three domain walls weakly form at high temperature ($T^* \sim 1.00$), although they are characterized by strong fluctuations in position and intensity. Upon further cooling, the domain walls assert their presence and a point defect becomes prominent in the sample ($T^* \sim 0.60$). As discussed in **Section 3.3**, due to the similarity between the two anchoring cases, it is only possible to distinguish the two samples by inspecting the relative arrangement of local directors in each sample.

4 CONCLUSION

Bulk and confined 2D samples were explored for the Gay-Berne mesogen with parameterization $GB(3, 5, 2, 1)$. This model calamitic exhibits a sharp isotropic-smectic (I-Sm) transition at lower pressures ($P^* < 2.0$); at higher pressures ($P^* \gtrsim 2.0$), the I-Sm transition involves an intermediate nematic phase. Clusters of locally ordered mesogens reach a threshold size, at sufficiently low temperatures, before the LC sample becomes smectic. The nematic phase shows an extended region of stability, nearly doubling in the temperature range at slightly lower densities. The critical point shifts to a lower temperature and a higher density compared to the analogous 3D system.

Confined samples were subjected to three boundary geometries: circular, square, and triangular. In *circular* geometry, two point defects emerge: for homeotropic anchoring, point defects are stable in the bulk region of the boundary and remain at a nearly constant separation. For

planar anchoring, point defects gravitate toward opposite poles of the boundary. In *square* geometry, no stable point defects are observed at low temperatures. Instead, two distinct domain walls give rise to three regions under homeotropic anchoring; the structure under planar anchoring results in four interconnecting domain walls, rhomboidal in form, producing five regions. In *triangular* geometry, confinement yields similar defects when comparing anchoring modes: three domain walls "emanate" from a nearly centered point defect yielding three regions. In this case, local directors must be accounted for to differentiate between anchoring modes.

All systems were studied with MD simulations. The resulting trajectories of confined 2D LC samples were visualized, revealing a complex evolution of textures originating from topological defects. Ordered domains at low temperatures are prefaced with strong thermal fluctuations that cause spatial variations in the mesophase at sufficiently high temperatures. Within the mesophase, flickering in position and intensity of topological defects is minimized at sufficiently low temperatures. Both the confining geometry and anchoring mode contribute to the type of defects observed.

Confined 2D LC systems provide a rich and exciting outlook. An outstanding matter with an eye toward 3D metamaterials is how disclinations couple when colloidal slabs are stacked. Practicable systems could extend layer-by-layer protocols [7, 89, 90, 168–180], thus expanding the gamut of metamaterials attainable by conventional 3D-based methods. Studies on the switching mechanics by applying external fields (as opposed to thermal tempering) would be of interest in the production of devices and associated technologies. A characterization of relevant timescales would offer an important perspective on design principles. Structured colloidal assemblies *via* topological defects could be exploited to yield colloidal assemblies with screw/twist properties, thus amplifying the availability of chiral materials.

DATA AVAILABILITY STATEMENT

The numerical model simulations upon which this study is based are unwieldy to archive or to transfer. Instead, all information needed to replicate the simulations is provided.

AUTHOR CONTRIBUTIONS

AC-A and JM-V performed bulk simulations, wrote post-simulation analysis codes, and implemented data analysis. AC-A carried out simulations for small-scale bulk samples as well as strongly confined systems and visualized trajectories. JM-V performed large-scale simulations of bulk samples *via* parallelization. SH and AR-H contributed to the interpretation of results and drafted relevant sections of the analysis. ES verified results for bulk systems, interpreted dynamical trajectories of strongly confined systems, and completed writing the manuscript. JM-R conceived the study, wrote the Gay-Berne simulation code, drafted initial versions of the manuscript, and coordinated the direction of the project.

SUPPLEMENTARY MATERIAL

The Supplementary Material for this article can be found online at: https://www.frontiersin.org/articles/10.3389/fphy.2020.622872/full#supplementary-material.

REFERENCES

1. Fedotov V. Springer Handbook of Electronic and Photonic Materials. 2nd ed. Cham, Switzerland: Springer International Publishing (2017). 1351–77. chap. Metamaterials.
2. Liu Y, Zhang X. Metamaterials: a new frontier of science and technology. *Chem Soc Rev* (2011) 40:2494–507. doi:10.1039/c0cs00184h
3. Whitesides GM, Love JC. The art of building small. *Sci Am* (2001) 285:38–47. doi:10.1038/scientificamerican0901-38
4. Zhang S. Building from the bottom up. *Mater Today* (2003) 6:20–7. doi:10.1016/s1369-7021(03)00530-3
5. Shimomura M, Sawadaishi T. Bottom-up strategy of materials fabrication: a new trend in nanotechnology of soft materials. *Curr Opin Colloid Interface Sci* (2001) 6:11–6. doi:10.1016/s1359-0294(00)00081-9
6. Kotnala A, Zheng Y. Digital assembly of colloidal particles for nanoscale manufacturing. *Part Part Syst Charact* (2002) 36:1900152. doi:10.1002/ppsc.201900152
7. Borges J, Mano JF. Molecular interactions driving the layer-by-layer assembly of multilayers. *Chem Rev* (2014) 114:8883–942. doi:10.1021/cr400531v
8. Conti S, Cecchini M. Predicting molecular self-assembly at surfaces: a statistical thermodynamics and modeling approach. *Phys Chem Chem Phys* (2016) 18:31480–93. doi:10.1039/c6cp05249e
9. Israelachvili JN. Intermolecular and Surface Forces. Amsterdam, Netherlands: Academic Press (2011). 503–76 p.
10. Vilfan M, Osterman N, Čopič M, Ravnik M, Žumer S, Kotar J, et al. Confinement effect on interparticle potential in nematic colloids. *Phys Rev Lett* (2008) 101:237801. doi:10.1103/PhysRevLett.101.237801
11. Tasinkevych M, Andrienko D. Colloidal particles in liquid crystal films and at interfaces. *Condens Matter Phys* (2010) 13:33603. doi:10.5488/cmp.13.33603
12. Verstraete L, Greenwood J, Hirsch BE, De Feyter S. Self-assembly under confinement: nanocorrals for understanding fundamentals of 2D crystallization. *ACS Nano* (2016) 10:10706–15. doi:10.1021/acsnano.6b05954
13. Pfeiffer CR, Pearce N, Champness NR. Complexity of two-dimensional self-assembled arrays at surfaces. *Chem Commun* (2017) 53:11528–39. doi:10.1039/c7cc06110b
14. Nieckarz D, Szabelski P. Surface-confined self-assembly of asymmetric tetratopic molecular building blocks. *Chem Phys Chem* (2019) 20:1850–9. doi:10.1002/cphc.201900344
15. Całus S, Busch M, Kityk AV, Piecek W, Huber P. Chiral phases of a confined cholesteric liquid crystal: anchoring-dependent helical and smectic self-assembly in nanochannels. *J Phys Chem C* (2016) 120:11727–38. doi:10.1021/acs.jpcc.6b03553
16. Whitesides GM. The once and future nanomachine. *Sci Am* (2001) 285:78–83.doi:10.1038/scientificamerican0901-78
17. Tu RS, Tirrell M. Bottom-up design of biomimetic assemblies. *Adv Drug Deliv Rev* (2004) 56:1537–63. doi:10.1016/j.addr.2003.10.047
18. Min Y, Akbulut M, Kristiansen K, Golan Y, Israelachvili J. The role of interparticle and external forces in nanoparticle assembly. *Nat Mater* (2008) 7:527–38. doi:10.1038/nmat2206
19. Muševič I. Nematic colloids, topology and photonics. *Philos Trans A Math Phys Eng Sci* (2013) 371:20120266. doi:10.1098/rsta.2012.0266
20. Lavrentovich OD. Liquid crystals, photonic crystals, metamaterials, and transformation optics. *Proc Natl Acad Sci U S A* (2011) 108:5143–4. doi:10.1073/pnas.1102130108
21. Muševič I, Škarabot M, Tkalec U, Ravnik M, Žumer S. Two-dimensional nematic colloidal crystals self-assembled by topological defects. *Science* (2006) 313:954–8. doi:10.1126/science.1129660
22. Alexander GP, Chen BGG, Matsumoto EA, Kamien RD. Colloquium: disclination loops, point defects, and all that in nematic liquid crystals. *Rev Mod Phys* (2012) 84:497–514. doi:10.1103/revmodphys.84.497
23. Čopar S, Porenta T, Jampani VSR, Muševič I, Žumer S. Stability and rewiring of nematic braids in chiral nematic colloids. *Soft Matter* (2012) 8:8595–600. doi:10.1039/C2SM25952D
24. Ravnik M, Alexander GP, Yeomans JM, Žumer S. Three-dimensional colloidal crystals in liquid crystalline blue phases. *Proc Natl Acad Sci U S A* (2011) 108:5188–92. doi:10.1073/pnas.1015831108
25. Nych A, Ognysta U, Škarabot M, Ravnik M, Žumer S, Muševič I. Assembly and control of 3D nematic dipolar colloidal crystals. *Nat Commun* (2013) 4:1489. doi:10.1038/ncomms2486
26. Poulin P, Stark H, Lubensky TC, Weitz DA. Novel colloidal interactions in anisotropic fluids. *Science* (1997) 275:1770–3. doi:10.1126/science.275.5307.1770
27. González-Martínez AD, Chávez-Rojo MA, Sambriski EJ, Moreno-Razo JA. Defect-mediated colloidal interactions in a nematic-phase discotic solvent. *RSC Adv* (2019) 9:33413–27. doi:10.1039/c9ra05377h
28. Martinez A, Hermosillo L, Tasinkevych M, Smalyukh, II. Linked topological colloids in a nematic host. *Proc Natl Acad Sci U S A* (2015) 112:4546–51. doi:10.1073/pnas.1500998112
29. Wang X, Miller DS, de Pablo JJ, Abbott NL. Reversible switching of liquid crystalline order permits synthesis of homogeneous populations of dipolar patchy microparticles. *Adv Funct Mater* (2014) 24:6219–26. doi:10.1002/adfm.201400911
30. Cavallaro M, Jr., Gharbi MA, Beller DA, Čopar S, Shi Z, Kamien RD, et al. Ring around the colloid. *Soft Matter* (2013) 9:9099–102. doi:10.1039/c3sm51167g
31. Liu Q, Senyuk B, Tasinkevych M, Smalyukh, II. Nematic liquid crystal boojums with handles on colloidal handlebodies. *Proc Natl Acad Sci U S A* (2013) 110:9231–6. doi:10.1073/pnas.1301464110
32. Čopar S, Tkalec U, Muševič I, Žumer S. Knot theory realizations in nematic colloids. *Proc Natl Acad Sci U S A* (2015) 112:1675–80. doi:10.1073/pnas.1417178112
33. Senyuk B, Liu Q, He S, Kamien RD, Kusner RB, Lubensky TC, et al. Topological colloids. *Nature* (2013) 493:200–5. doi:10.1038/nature11710
34. Araki T, Tanaka H. Colloidal aggregation in a nematic liquid crystal: topological arrest of particles by a single-stroke disclination line. *Phys Rev Lett* (2006) 97:127801. doi:10.1103/PhysRevLett.97.127801
35. Ravnik M, Škarabot M, Žumer S, Tkalec U, Poberaj I, Babic D, et al. Entangled nematic colloidal dimers and wires. *Phys Rev Lett* (2007) 99:247801. doi:10.1103/PhysRevLett.99.247801
36. Jampani VS, Škarabot M, Ravnik M, Čopar S, Žumer S, Muševič I. Colloidal entanglement in highly twisted chiral nematic colloids: twisted loops, Hopf

links, and trefoil knots. *Phys Rev E—Stat Nonlinear Soft Matter Phys* (2011) 84: 031703. doi:10.1103/PhysRevE.84.031703

37. Hashemi SM, Ravnik M. Nematic colloidal knots in topological environments. *Soft Matter* (2018) 14:4935–45. doi:10.1039/c8sm00539g

38. Tkalec U, Ravnik M, Čopar S, Žumer S, Muševič I. Reconfigurable knots and links in chiral nematic colloids. *Science* (2011) 333:62–5. doi:10.1126/science.1205705

39. Lubensky TC, Pettey D, Currier N, Stark H. Topological defects and interactions in nematic emulsions. *Phys Rev E* (1998) 57:610–25. doi:10.1103/physreve.57.610

40. Loudet JC, Barois P, Poulin P. Colloidal ordering from phase separation in a liquid-crystalline continuous phase. *Nature* (2000) 407:611–3. doi:10.1038/35036539

41. Wang X, Miller DS, Bukusoglu E, de Pablo JJ, Abbott NL. Topological defects in liquid crystals as templates for molecular self-assembly. *Nat Mater* (2016) 15:106–12. doi:10.1038/nmat4421

42. Smalyukh II, Lavrentovich OD, Kuzmin AN, Kachynski AV, Prasad PN. Elasticity-mediated self-organization and colloidal interactions of solid spheres with tangential anchoring in a nematic liquid crystal. *Phys Rev Lett* (2005) 95: 157801–4. doi:10.1103/PhysRevLett.95.157801

43. Gharbi MA, Nobili M, Blanc C. Use of topological defects as templates to direct assembly of colloidal particles at nematic interfaces. *J Colloid Interface Sci* (2014) 417:250–5. doi:10.1016/j.jcis.2013.11.051

44. Pandey MB, Porenta T, Brewer J, Burkart A, Copar S, Žumer S, et al. Self-assembly of skyrmion-dressed chiral nematic colloids with tangential anchoring. *Phys Rev E—Stat Nonlinear Soft Matter Phys* (2014) 89:060502. doi:10.1103/PhysRevE.89.060502

45. Kim JH, Yoneya M, Yokoyama H. Tristable nematic liquid-crystal device using micropatterned surface alignment. *Nature* (2002) 420:159–62. doi:10.1038/nature01163

46. Machon T, Alexander GP. Knots and nonorientable surfaces in chiral nematics. *Proc Natl Acad Sci U. S. A* (2013) 110:14174–9.doi:10.1073/pnas.1308225110

47. Frydel D, Rice SA. Phase diagram of a quasi-two-dimensional colloid assembly. *Phys Rev E—Stat Nonlinear Soft Matter Phys* (2003) 68:061405. doi:10.1103/PhysRevE.68.061405

48. Fomin YD, Ryzhov VN, Tsiok EN. The influence of long-range interaction on the structure of a two-dimensional multi scale potential system. *J Phys Condens Matter* (2019) 31:315103. doi:10.1088/1361-648x/ab1df6

49. Fomin YD. The phase diagram of a two-dimensional core-softened system with purely repulsive monotonic potential. *Phys Stat Mech Appl* (2021) 565: 125519. doi:10.1016/j.physa.2020.125519

50. Li B, Xiao X, Wang S, Wen W, Wang Z. Real-space mapping of the two-dimensional phase diagrams in attractive colloidal systems. *Phys Rev X* (2019) 9:031032. doi:10.1103/physrevx.9.031032

51. Zhu X, Truskett TM, Bonnecaze RT. Phase diagram for two-dimensional layer of soft particles. *Soft Matter* (2019) 15:4162–9. doi:10.1039/c9sm00333a

52. Dudalov DE, Fomin YD, Tsiok EN, Ryzhov VN. How dimensionality changes the anomalous behavior and melting scenario of a core-softened potential system? *Soft Matter* (2014) 10:4966–76. doi:10.1039/c4sm00124a

53. Kryuchkov NP, Yurchenko SO, Fomin YD, Tsiok EN, Ryzhov VN. Complex crystalline structures in a two-dimensional core-softened system. *Soft Matter* (2018) 14:2152–62. doi:10.1039/c7sm02429k

54. Padilla LA, Ramírez-Hernández A. Phase behavior of a two-dimensional core-softened system: new physical insights. *J Phys Condens Matter* (2020a) 32: 275103. doi:10.1088/1361-648x/ab7e5c

55. Padilla LA, Ramírez-Hernández A. Phase diagrams of simple models of colloidal nanocrystals in two dimensions. *J Phys Mater* (2020b) 4:015006. doi:10.1088/2515-7639/abc7ed

56. Harth K, Stannarius R. Topological point defects of liquid crystals in quasi-two-dimensional geometries. *Front Physiol* (2020) 8:112. doi:10.3389/fphy.2020.00112

57. Hogan BT, Kovalska E, Craciun MF, Baldycheva A. 2D material liquid crystals for optoelectronics and photonics. *J Mater Chem C* (2017) 5:11185–95. doi:10.1039/c7tc02549a

58. Al-Zangana S, Iliut M, Turner M, Vijayaraghavan A, Dierking I. Properties of a thermotropic nematic liquid crystal doped with graphene oxide. *Adv Optical Mater* (2016) 4:1541. doi:10.1002/adom.201600351

59. Lavrič M, Cordoyiannis G, Tzitzios V, Lelidis I, Kralj S, Nounesis G, et al. Blue phase stabilization by CoPt-decorated reduced-graphene oxide nanosheets dispersed in a chiral liquid crystal. *J Appl Phys* (2020) 127:095101. doi:10.1063/1.5141930

60. Wang L, Urbas AM, Li Q. Nature-inspired emerging chiral liquid crystal nanostructures: from molecular self-assembly to DNA mesophase and nanocolloids. *Adv Mater* (2020) 32:1801335. doi:10.1002/adma.201801335

61. Li P, Wong M, Zhang X, Yao H, Ishige R, Takahara A, et al. Tunable lyotropic photonic liquid crystal based on graphene oxide. *ACS Photonics* (2014) 1: 79–86. doi:10.1021/ph400093c

62. Oaki Y. Intercalation and flexibility chemistries of soft layered materials. *Chem Commun* (2020) 56:13069–81. doi:10.1039/d0cc05931e

63. Querejeta-Fernández A, Chauve G, Methot M, Bouchard J, Kumacheva E. Chiral plasmonic films formed by gold nanorods and cellulose nanocrystals. *J Am Chem Soc* (2014) 136:4788–93. doi:10.1021/ja501642p

64. Atorf B, Funck T, Hegmann T, Kempter S, Liedl T, Martens K, et al. Liquid crystals and precious metal: from nanoparticle dispersions to functional plasmonic nanostructures. *Liq Cryst* (2017) 44:1929–47. doi:10.1080/02678292.2017.1359692

65. Boles MA, Engel M, Talapin DV. Self-assembly of colloidal nanocrystals: from intricate structures to functional materials. *Chem Rev* (2016) 116:11220–89. doi:10.1021/acs.chemrev.6b00196

66. Bedolla Pantoja MA, Abbott NL. Surface-controlled orientational transitions in elastically strained films of liquid crystal that are triggered by vapors of toluene. *ACS Appl Mater Interfaces* (2016) 8:13114–22. doi:10.1021/acsami.6b02139

67. Ishihara S, Lee JJ, Kek KJ. Detection of volatile organic chemicals by using liquid crystals. *IET Mater Circuits Devices Ser* (2019) 68:315–40. doi:10.1049/pbcs068g_ch19

68. Shibaev PV, Wenzlick M, Murray J, Tantillo A, Howard-Jennings J. Rebirth of liquid crystals for sensoric applications: environmental and gas sensors. *Adv Condens Matter Phys* (2015) 2015:729186. doi:10.1155/2015/729186

69. Chari K, Rankin CM, Johnson DM, Blanton TN, Capurso RG. Single-substrate cholesteric liquid crystal displays by colloidal self-assembly. *Appl Phys Lett* (2006) 88:043502. doi:10.1063/1.2167398

70. Draude AP, Kalavalapalli TY, Iliut M, McConnell B, Dierking I. Stabilization of liquid crystal blue phases by carbon nanoparticles of varying dimensionality. *Nanoscale Adv* (2020) 2:2404–9. doi:10.1039/d0na00276c

71. Ge Z, Rao L, Gauza S, Wu S-T. Modeling of blue phase liquid crystal displays. *J Disp Technol* (2009) 5:250–6. doi:10.1109/jdt.2009.2022849

72. Kakiuchida H, Ogiwara A. Smart windows. *IET Mater Circuits Devices Ser* (2019) 68:341–59. doi:10.1049/pbcs068g_ch20

73. Stratford K, Henrich O, Lintuvuori JS, Cates ME, Marenduzzo D. Self-assembly of colloid-cholesteric composites provides a possible route to switchable optical materials. *Nat Commun* (2014) 5:3954. doi:10.1038/ncomms4954

74. Ng AY, See CW, Somekh MG. Quantitative optical microscope with enhanced resolution using a pixelated liquid crystal spatial light modulator. *J Microsc* (2004) 214:334–40. doi:10.1111/j.0022-2720.2004.01323.x

75. Bergamini S, Darquié B, Jones M, Jacubowiez L, Browaeys A, Grangier P. Holographic generation of microtrap arrays for single atoms by use of a programmable phase modulator. *J Opt Soc Am B* (2004) 21:1889–94. doi:10.1364/josab.21.001889

76. Smith PJ, Taylor CM, Shaw AJ, McCabe EM. Programmable array microscopy with a ferroelectric liquid-crystal spatial light modulator. *Appl Optic* (2000) 39: 2664–9. doi:10.1364/ao.39.002664

77. Capeluto MG, La Mela C, Iemmi C, Marconi MC. Scanning mechanism based on a programmable liquid crystal display. *Optic Commun* (2004) 232:107–13. doi:10.1016/j.optcom.2003.12.080

78. Bunning TJ, Natarajan LV, Tondiglia VP, Sutherland RL. Holographic polymer-dispersed liquid crystals (H-PDLCs). *Annu Rev Mater Sci* (2000) 30:83–115. doi:10.1146/annurev.matsci.30.1.83

79. Qi J, Li L, De Sarkar M, Crawford GP. Nonlocal photopolymerization effect in the formation of reflective holographic polymer-dispersed liquid crystals. *J Appl Phys* (2004) 96:2443–50. doi:10.1063/1.1778480

80. Bowley CC, Kossyrev PA, Crawford GP, Faris S. Variable-wavelength switchable Bragg gratings formed in polymer-dispersed liquid crystals. *Appl Phys Lett* (2001) 79:9–11. doi:10.1063/1.1383566

81. Chen C-Y, Pan C-L, Hsieh C-F, Lin Y-F, Pan R-P. Liquid-crystal-based terahertz tunable Lyot filter. *Appl Phys Lett* (2006) 88:101107. doi:10.1063/1.2181271

82. Peierls R. Surprises in Theoretical Physics. Princeton, NJ: Princeton University Press (1979). p 85–91.

83. Ryzhov VN, Gaiduk EA, Tareyeva EE, Fomin YD, Tsiok EN. The Berezinskii-Kosterlitz-Thouless transition and melting scenarios of two-dimensional systems. *Phys Part Nucl* (2020) 51:786–90. doi:10.1134/s1063779620040632

84. Kosterlitz JM, Thouless DJ. Ordering, metastability and phase transitions in two-dimensional systems. *J Phys C Solid State Phys* (2002) 6:1181–203. doi:10.1088/0022-3719/6/7/010

85. Bak P, Paczuski M. Chapter 1 - Principles of Phase Transitions in Two-dimensional Systems. In: DA King DP. Woodruff, editors *Phase transitions and adsorbate restructuring at metal surfaces*. Amsterdam, Netherlands: Elsevier. The Chemical Physics of Solid Surfaces (1994), Vol. 7. p. 1–33. doi:10.1016/B978-0-444-81924-6.50006-0

86. Mermin ND. Crystalline order in two dimensions. *Phys Rev* (1968) 176:250–4. doi:10.1103/PhysRev.176.250

87. Kumari S, Ye F, Podgornik R. Ordering of adsorbed rigid rods mediated by the Boussinesq interaction on a soft substrate. *J Chem Phys* (2020) 153:144905. doi:10.1063/5.0022556

88. Wang W, Lin J-T, Su Y-S, I L. Micro-structure and motion of two-dimensional dense short spherocylinder liquids. *J Phys Condens Matter* (2018) 30:125102. doi:10.1088/1361-648x/aaaf03

89. Batys P, Nosek M, Weroński P. Structure analysis of layer-by-layer multilayer films of colloidal particles. *Appl Surf Sci* (1999) 332:318–27. doi:10.1016/j.apsusc.2015.01.171

90. Jalili R, Aboutalebi SH, Esrafilzadeh D, Konstantinov K, Moulton SE, Razal JM, et al. Organic solvent-based graphene oxide liquid crystals: a facile route toward the next generation of self-assembled layer-by-layer multifunctional 3D architectures. *ACS Nano* (2013) 7:3981–90. doi:10.1021/nn305906z

91. Jasieniak JJ, MacDonald BI, Mulvaney P. Nanocrystals, Layer-by-Layer Assembly, and Photovoltaic Devices. Wiley (2015). p. 357–94. Chap. 14. doi:10.1002/9781118867204.ch14

92. Gay JG, Berne BJ. Modification of the overlap potential to mimic a linear site-site potential. *J Chem Phys* (1981) 74:3316–9. doi:10.1063/1.441483

93. Memmer R, Kuball H-G, Schönhofer A. Computer simulation of chiral liquid crystal phases. I. The polymorphism of the chiral Gay-Berne fluid. *Liq Cryst* (1993) 15:345–60. doi:10.1080/02678299308029136

94. Memmer R, Janssen F. Computer simulation of chiral liquid crystal phases IX. Chiral induction in guest-host systems—calculation of the helical twisting power. *Z Naturforsch* (2014) 54:747–54. 10.1515/zna-1999-1212

95. Luckhurst GR, Stephens RA, Phippen RW. Computer simulation studies of anisotropic systems. XIX. Mesophases formed by the Gay-Berne model mesogen. *Liq Cryst* (1990) 8:451–64. doi:10.1080/02678299008047361

96. Satoh K, Mita S, Kondo S. Monte Carlo simulations on mesophase formation using dipolar Gay-Berne model. *Liq Cryst* (1996) 20:757–63. doi:10.1080/02678299608033169

97. Luckhurst GR, Luckhurst GR, Stephens RA, Phippen RW. The Gay-Berne mesogen: a paradigm shift? *Liq Cryst* (2006) 33:1389–405. doi:10.1080/02678290601140456

98. Bartsch H, Bier M, Dietrich S. Interface structures in ionic liquid crystals. *Soft Matter* (2019) 15:4109–26. doi:10.1039/c9sm00062c

99. Salgado-Blanco D, Díaz-Herrera E, Mendoza CI. Effect of the anchoring strength on the phase behaviour of discotic liquid crystals under face-on confinement. *J Phys Condens Matter* (2019) 31:105101. doi:10.1088/1361-648x/aaf843

100. Nozawa T, Brumby PE, Ayuba S, Yasuoka K. Ordering in clusters of uniaxial anisotropic particles during homogeneous nucleation and growth. *J Chem Phys* (2019) 150:054903. doi:10.1063/1.5064410

101. Segatti A, Snarski M, Veneroni M. Equilibrium configurations of nematic liquid crystals on a torus. *Phys Rev E—Stat Nonlinear Soft Matter Phys* (2014) 90:012501. doi:10.1103/PhysRevE.90.012501

102. Cañeda-Guzmán E, Moreno-Razo JA, Díaz-Herrera E, Sambriski EJ. Molecular aspect ratio and anchoring strength effects in a confined Gay-Berne liquid crystal. *Mol Phys* (2014) 112:1149–59. doi:10.1080/00268976.2013.837206

103. Margola T, Satoh K, Saielli G. Comparison of the mesomorphic behaviour of 1:1 and 1:2 mixtures of charged Gay-Berne GB(4.4,20.0,1,1) and Lennard-Jones particles. *Crystals* (2018) 8:3711–5.doi:10.3390/cryst8100371

104. de Miguel E, Martín del Río E, Blas FJ. Stability of smectic phases in the Gay-Berne model. *J Chem Phys* (2004) 121:11183–94. doi:10.1063/1.1810472

105. Cienega-Cacerez O, Moreno-Razo JA, Díaz-Herrera E, Sambriski EJ. Phase equilibria, fluid structure, and diffusivity of a discotic liquid crystal. *Soft Matter* (2014) 10:3171–82. doi:10.1039/c3sm52301b

106. Cienega-Cacerez O, García-Alcántara C, Moreno-Razo JA, Díaz-Herrera E, Sambriski EJ. Induced stabilization of columnar phases in binary mixtures of discotic liquid crystals. *Soft Matter* (2016) 12:1295–312. doi:10.1039/c5sm01959a

107. Caprion D, Bellier-Castella L, Ryckaert JP. Influence of shape and energy anisotropies on the phase diagram of discotic molecules. *Phys Rev E—Stat Nonlinear Soft Matter Phys* (2003) 67:041703. doi:10.1103/PhysRevE.67.041703

108. Bates MA, Luckhurst GR. Computer simulation studies of anisotropic systems. XXVI. Monte Carlo investigations of a Gay-Berne discotic at constant pressure. *J Chem Phys* (1996) 104:6696–709. doi:10.1063/1.471387

109. Patti A, Belli S, van Roij R, Dijkstra M. Relaxation dynamics in the columnar liquid crystal phase of hard platelets. *Soft Matter* (2011) 7:3533–45. doi:10.1039/c0sm01265c

110. Thompson IR, Coe MK, Walker AB, Ricci M, Roscioni OM, Zannoni C. Microscopic origins of charge transport in triphenylene systems. *Phys Rev Mater* (2018) 2:064601. doi:10.1103/physrevmaterials.2.064601

111. Cammidge AN, Bushby RJ. Handbook of liquid crystals, Synthesis and Structural Features. Chap. VII, Vol. 2B. Weinheim, Germany: Oxford University Press (1998). p. 703–5. doi:10.1002/9783527620623.ch4

112. Phillips TJ, Jones JC, McDonnell DG. On the influence of short range order upon the physical properties of triphenylene nematic discogens. *Liq Cryst* (1993) 15:203–15. doi:10.1080/02678299308031951

113. Kundu P, Mishra P, Jaiswal A, Ram J. Structures and phase transition in a two-dimensional system of Gay-Berne molecules. *J Mol Liq* (2019) 296:111769. doi:10.1016/j.molliq.2019.111769

114. Kundu P, Mishra P. Simulation of Gay-Berne liquid crystal molecules confined to a plane. *AIP Conf Proc* (2020) 2220:130016. doi:10.1063/5.0001132

115. Jordens S, Isa L, Usov I, Mezzenga R. Non-equilibrium nature of two-dimensional isotropic and nematic coexistence in amyloid fibrils at liquid interfaces. *Nat Commun* (2013) 4:1917. doi:10.1038/ncomms2911

116. Zheng Z, Wang F, Han Y. Glass transitions in quasi-two-dimensional suspensions of colloidal ellipsoids. *Phys Rev Lett* (2011) 107:065702. doi:10.1103/PhysRevLett.107.065702

117. Cortes LB, Gao Y, Dullens RP, Aarts DG. Colloidal liquid crystals in square confinement: isotropic, nematic and smectic phases. *J Phys Condens Matter* (2017) 29:064003. doi:10.1088/1361-648X/29/6/064003

118. Gârlea IC, Mulder P, Alvarado J, Dammone O, Aarts DG, Lettinga MP, et al. Finite particle size drives defect-mediated domain structures in strongly confined colloidal liquid crystals. *Nat Commun* (2016) 7:12112. doi:10.1038/ncomms12112

119. de las Heras D, Velasco E, Mederos L. Topological defects in a two-dimensional liquid crystal confined in a circular nanocavity. *Phys Rev E-Stat Nonlinear Soft Matter Phys* (2009) 79:061703. doi:10.1103/PhysRevE.79.061703

120. González-Pinto M, Martínez-Ratón Y, Velasco E. Liquid-crystal patterns of rectangular particles in a square nanocavity. *Phys Rev E-Stat Nonlinear Soft Matter Phys* (2013) 88:032506. doi:10.1103/PhysRevE.88.032506

121. Yao X, Zhang H, Chen JZY. Topological defects in two-dimensional liquid crystals confined by a box. *Phys Rev E* (2018) 97:052707. doi:10.1103/PhysRevE.97.052707

122. Walton J, Mottram NJ, McKay G. Nematic liquid crystal director structures in rectangular regions. *Phys Rev E* (2018) 97:022702. doi:10.1103/PhysRevE.97.022702

123. Foulaadvand ME, Yarifard M. Two-dimensional system of hard ellipses: a molecular dynamics study. *Phys Rev E-Stat Nonlinear Soft Matter Phys* (2013) 88:052504. doi:10.1103/PhysRevE.88.052504

124. de las Heras D, Velasco E. Domain walls in two-dimensional nematics confined in a small circular cavity. *Soft Matter* (2014) 10:1758–66. doi:10.1039/c3sm52650j

125. Geigenfeind T, Rosenzweig S, Schmidt M, de Las Heras D. Confinement of two-dimensional rods in slit pores and square cavities. *J Chem Phys* (2015) 142:174701. doi:10.1063/1.4919307

126. Gârlea IC, Mulder BM. Defect structures mediate the isotropic-nematic transition in strongly confined liquid crystals. *Soft Matter* (2015) 11:608–14. doi:10.1039/c4sm02087a

127. Sidky H, Whitmer JK. Elastic properties of common Gay-Berne nematogens from density of states (DOS) simulations. *Liq Cryst* (2016) 43:2285–99. doi:10.1080/02678292.2016.1201869

128. de Miguel E, Rull LF, Chalam MK, Gubbins KE. Liquid crystal phase diagram of the Gay-Berne fluid. *Mol Phys* (1991) 74:405–24. doi:10.1080/00268979100102321

129. Brown JT, Allen MP, Martín del Río E, de Miguel E. Effects of elongation on the phase behavior of the Gay-Berne fluid. *Phys Rev E* (1998) 57:6685–99. doi:10.1103/physreve.57.6685

130. Bates MA, Luckhurst GR. Computer Simulation of Liquid Crystal Phases Formed by Gay-Berne Mesogens. Liquid Crystals I. Berlin, Heidelberg: Springer Berlin Heidelberg (1999). p. 65–137. doi:10.1007/3-540-68305-4_3

131. de Miguel E. Reexamining the phase diagram of the Gay-Berne fluid. *Mol Phys* (2002) 100:2449–59. doi:10.1080/00268970210121605

132. de Miguel E, Vega C. The global phase diagram of the Gay-Berne model. *J Chem Phys* (2002) 117:6313–22. doi:10.1063/1.1504430

133. Allen MP, Warren MA, Wilson MR, Sauron A, Smith W. Molecular dynamics calculation of elastic constants in Gay-Berne nematic liquid crystals. *J Chem Phys* (1996) 105:2850–8. doi:10.1063/1.472147

134. Joshi AA, Whitmer JK, Guzmán O, Abbott NL, de Pablo JJ. Measuring liquid crystal elastic constants with free energy perturbations. *Soft Matter* (2014) 10:882–93. doi:10.1039/c3sm51919h

135. Humpert A, Allen MP. Elastic constants and dynamics in nematic liquid crystals. *Mol Phys* (2015) 113:2680–92.doi:10.1080/00268976.2015.1067730

136. Stillings C, Martin E, Steinhart M, Pettau R, Paraknowitsch J, Geuss M, et al. Nanoscaled discotic liquid crystal/polymer systems: confinement effects on morphology and thermodynamics. *Mol Cryst Liq Cryst* (2008) 495:285–292. doi:10.1080/15421400802430349

137. Caprion D. Discotic molecules in cylindrical nanopores: a Monte Carlo study. *Eur Phys J E Soft Matter* (2009) 28:305–13.doi:10.1140/epje/i2008-10412-6

138. Busselez R, Cerclier CV, Ndao M, Ghoufi A, Lefort R, Morineau D. Discotic columnar liquid crystal studied in the bulk and nanoconfined states by molecular dynamics simulation. *J Chem Phys* (2014) 141:134902. doi:10.1063/1.4896052

139. Sentker K, Zantop AW, Lippmann M, Hofmann T, Seeck OH, Kityk AV, et al. Quantized self-assembly of discotic rings in a liquid crystal confined in nanopores. *Phys Rev Lett* (2018) 120:067801. doi:10.1103/PhysRevLett.120.067801

140. Salgado-Blanco D, Mendoza CI, Chávez-Rojo MA, Moreno-Razo JA, Díaz-Herrera E. Influence of anchoring in the phase behaviour of discotic liquid crystals. *Soft Matter* (2018) 14:2846–59. doi:10.1039/c7sm02311a

141. Rull LF, Romero-Enrique JM. Nanodrops of discotic liquid crystals: a Monte Carlo study. *Langmuir* (2017a) 33:11779–87. doi:10.1021/acs.langmuir.7b02347

142. Humpert A, Masters AJ, Allen MP. Orientational dynamics in nematic liquid crystals. *Eur Phys J Spec Top* (2016) 225:1723–32. doi:10.1140/epjst/e2016-60118-1

143. Allen MP. Molecular simulation of liquid crystals. *Mol Phys* (2019) 117:2391–417. doi:10.1080/00268976.2019.1612957

144. Rull LF, Romero-Enrique JM. Computer simulation study of the nematic-vapour interface in the Gay-Berne model. *Mol Phys* (2017b) 115:1214–24. doi:10.1080/00268976.2016.1274437

145. Wilson MR. Progress in computer simulations of liquid crystals. *Int Rev Phys Chem* (2005) 24:421–55. doi:10.1080/01442350500361244

146. Mishra P, Ram J. Effect of shape anisotropy on the phase diagram of the Gay-Berne fluid. *Eur Phys J E Soft Matter* (2005) 17:345–51.doi:10.1140/epje/i2005-10014-x

147. Berne BJ, Pechukas P. Gaussian model potentials for molecular interactions. *J Chem Phys* (1972) 56:4213–6. doi:10.1063/1.1677837

148. Cleaver DJ, Care CM, Allen MP, Neal MP. Extension and generalization of the Gay-Berne potential. *Phys Rev E* (1996) 54:559–67. doi:10.1103/physreve.54.559

149. Antypov D, Cleaver DJ. The effect of spherical additives on a liquid crystal colloid. *J Phys Condens Matter* (2004) 16:S1887–S1900. doi:10.1088/0953-8984/16/19/002

150. Frenkel D, Smit B, eds. Understanding Molecular Simulation: From Algorithms to Applications. 1st ed. Orlando, FL: Academic Press, Inc. (1996).

151. Gruhn T, Schoen M. Microscopic structure of molecularly thin confined liquid-crystal films. *Phys Rev E* (1997) 55:2861–75. doi:10.1103/physreve.55.2861

152. de Gennes PG. The Physics of Liquid Crystals. Oxford, United Kingdom: Clarendon Press (1993).

153. Cuesta JA, Frenkel D. Monte Carlo simulation of two-dimensional hard ellipses. *Phys Rev* (1990) 42:2126–36. doi:10.1103/physreva.42.2126

154. Illing B, Fritschi S, Kaiser H, Klix CL, Maret G, Keim P. Mermin-Wagner fluctuations in 2D amorphous solids. *Proc Natl Acad Sci U S A* (2017) 114:1856–61. doi:10.1073/pnas.1612964114

155. Flenner E, Szamel G. Fundamental differences between glassy dynamics in two and three dimensions. *Nat Commun* (2015) 6:7392. doi:10.1038/ncomms8392

156. Verbeck B. 2D materials: amorphous and fluctuating. *Nat Phys* (2017) 13:205. doi:10.1038/nphys4065

157. Wegner FJ. Corrections to scaling laws. *Phys Rev B* (1972) 5:4529–36. doi:10.1103/physrevb.5.4529

158. Armas-Pérez JC, Quintana HJ, Chapela GA. Liquid-vapor equilibrium and interfacial properties of square wells in two dimensions. *J Chem Phys* (2013) 138:044508. doi:10.1063/1.4775342

159. Panagiotopoulos AZ. Direct determination of phase coexistence properties of fluids by Monte Carlo simulation in a new ensemble. *Mol Phys* (1987) 61:813–26. doi:10.1080/00268978700101491

160. Bates MA, Frenkel D. Nematic-isotropic transition in polydisperse systems of infinitely thin hard platelets. *J Chem Phys* (1999) 110:6553–9. doi:10.1063/1.478558

161. Bianchi E, Tartaglia P, Zaccarelli E, Sciortino F. Theoretical and numerical study of the phase diagram of patchy colloids: ordered and disordered patch arrangements. *J Chem Phys* (2008) 128:144504. doi:10.1063/1.2888997

162. Kofke DA. Gibbs-Duhem integration: a new method for direct evaluation of phase coexistence by molecular simulation. *Mol Phys* (1993) 78:1331–6. doi:10.1080/00268979300100881

163. Ferrenberg AM, Swendsen RH. New Monte Carlo technique for studying phase transitions. *Phys Rev Lett* (1988) 61:2635–8. doi:10.1103/PhysRevLett.61.2635

164. Frenkel D, Ladd AJC. New Monte Carlo method to compute the free energy of arbitrary solids. Application to the fcc and hcp phases of hard spheres. *J Chem Phys* (1984) 81:3188–93. doi:10.1063/1.448024

165. Selinger JV. Introduction to the Theory of Soft Matter: From Ideal Gases to Liquid Crystals. Cham, Switzerland: Springer (2016). p 99.

166. Robinson M, Luo C, Farrell PE, Erban R, Majumdar A. From molecular to continuum modelling of bistable liquid crystal devices. *Liq Cryst* (2017) 44:2267–84. doi:10.1080/02678292.2017.1290284

167. Guillamat P, Ignés-Mullol J, Sagués F. Control of active liquid crystals with a magnetic field. *Proc Natl Acad Sci U S A* (2016) 113:5498–502. doi:10.1073/pnas.1600339113

168. Wågberg L, Erlandsson J. The use of layer-by-layer self-assembly and nanocellulose to prepare advanced functional materials. *Adv Mater* (2020) 32:2001474. doi:10.1002/adma.202001474

169. Konopelnyk OI, Aksimentyeva OI, Horbenko YY, Poliovyi DO, Opaynych IY. Layer-by-layer assembly and thermal sensitivity of poly(3,4-ethylenedioxythiophene) nanofilms. *Mol Cryst Liq Cryst* (2016) 640:158–64. doi:10.1080/15421406.2016.1257327

170. Amabilino DB. Supramolecular Chemistry at Surfaces (the Royal Society of Chemistry), chapter 6. Layer-by-layer growth. *Monographs Supramol Chem* (2016):303–39. doi:10.1039/9781782622161-00303

171. Lee T, Min SH, Gu M, Jung YK, Lee W, Lee JU, et al. Layer-by-Layer assembly for graphene-based multilayer nanocomposites: synthesis and applications. *Chem Mater* (2015) 27:3785–96. doi:10.1021/acs.chemmater.5b00491

172. Tjipto E, Cadwell KD, Quinn JF, Johnston AP, Abbott NL, Caruso F. Tailoring the interfaces between nematic liquid crystal emulsions and aqueous phases via layer-by-layer assembly. *Nano Lett* (2006) 6:2243–8. doi:10.1021/nl061604p

173. Richardson JJ, Björnmalm M, Caruso F. Multilayer assembly. Technology-driven layer-by-layer assembly of nanofilms. *Science* (2015) 348:aaa2491. doi:10.1126/science.aaa2491

174. Zhang X, Chen H, Zhang H. Layer-by-layer assembly: from conventional to unconventional methods. *Chem Commun* (2007) 1395–405. doi:10.1039/b615590a

175. Ariga K, Hill JP, Ji Q. Layer-by-layer assembly as a versatile bottom-up nanofabrication technique for exploratory research and realistic application. *Phys Chem Chem Phys* (2007) 9:2319–40. doi:10.1039/b700410a

176. Tian W, VahidMohammadi A, Wang Z, Ouyang L, Beidaghi M, Hamedi MM. Layer-by-layer self-assembly of pillared two-dimensional multilayers. *Nat Commun* (2019) 10:2558. doi:10.1038/s41467-019-10631-0

177. Wang AC, Pereira I, Ferreira C, Veiga F, Fakhrullin R. Chapter 1.4 - Layer-by-Layer Assembly for Nanoarchitectonics. In: K Ariga M. Aono, editors. Norwich, NY: William Andrew Publishing, Micro and Nano Technologies (2019). p. 89–121. doi:10.1016/B978-0-12-813341-5.00005-X

178. Zhao S, Caruso F, Dähne L, Decher G, De Geest BG, Fan J, et al. The future of layer-by-layer assembly: a tribute to ACS Nano associate editor Helmuth Möhwald. *ACS Nano* (2019) 13:6151–69. doi:10.1021/acsnano.9b03326

179. Oliveira DA, Gasparotto LHS, Siqueira JR, Jr. Processing of nanomaterials in Layer-by-Layer films: potential applications in (bio)sensing and energy storage. *An Acad Bras Cienc* (2019) 91:e20181343. doi:10.1590/0001-3765201920181343

180. Moon G, Jang W, Son I, Cho H, Park Y, Lee J. Fabrication of new liquid crystal device using layer-by-layer thin film process. *Processes* (2018) 6:108. doi:10.3390/pr6080108